

Bistability in spatiotemporal mode-locking with dynamic multimode gain

ZHIJIN XIONG,^{1,3} YUANKAI GUO,^{1,3} WEI LIN,^{1,3} HAO XIU,¹ YUNCONG MA,¹ XUEWEN CHEN,¹ ZHAOHENG LIANG,¹ LIN LING,¹ TAO LIU,¹ XIAOMING WEI,^{1*} AND ZHONGMIN YANG^{1,2*}

¹*School of Physics and Optoelectronics, State Key Laboratory of Luminescent Materials and Devices, Guangdong Engineering Technology Research and Development Center of Special Optical Fiber Materials and Devices, Guangdong Provincial Key Laboratory of Fiber Laser Materials and Applied Techniques, South China University of Technology, Guangzhou 510640, China*

²*Research Institute of Future Technology, South China Normal University, Guangzhou 510006, China*

³*These authors equally contributed to this work.*

**email: xmwei@scut.edu.cn; yangzm@scut.edu.cn*

Abstract: Three-dimensional (3D) dissipative soliton existed in spatiotemporal mode-locked (STML) multimode fiber laser has been demonstrated to be a promising formalism for generating high-energy femtosecond pulses, which unfortunately exhibit diverse spatiotemporal dynamics that have not been fully understood. Completely modeling the STML multimode fiber lasers can shed new light on the underlying physics of the spatiotemporal dynamics and thus better manipulate the generation of high-quality energetic femtosecond pulses, which however is still largely unmet. To this end, here we theoretically investigate a dynamic multimode gain model of the STML multimode fiber laser by exploring the multimode rate equation (MMRE) in the framework of generalized multimode nonlinear Schrödinger equation. Using this dynamic multimode gain model, the attractor dissection theory is revisited to understand the dominant effects that determine the modal composition of 3D dissipative soliton. Specifically, by varying the numerical aperture of the multimode gain fiber (MMGF), different gain dynamics that correspond to distinct types of gain attractors are observed. As a result, two distinguishing STML operation regimes, respectively governed by the multimode gain effect and spatiotemporal saturable absorption, are identified. In the latter regime, especially, 3D dissipative solitons present bistability that there exist bifurcated solutions with two different linearly polarized (LP) mode compositions. To verify the theoretical findings, the experimental implementation shows that the state of STML can be switched between different LP modes, and confirms the presence of bistability. Particularly, the 3D-soliton shaping mechanism that is governed by the multimode gain effect is testified for the first time, to the best of our knowledge. It is anticipated that the proposed dynamic multimode gain model can create new potential for studying the complexity of 3D dissipative soliton.

1. Introduction

Mode-locked fiber lasers have been intensively investigated in the past decades for their high beam quality, reliability, excellent thermal management, compact design, ease of use, etc [1,2]. Different from the traditional single-mode counterparts, the study of mode-locked multimode fiber lasers is challenging due to the complicated interplay between the transverse and longitudinal modes [3]. Ever since the first demonstration of spatiotemporal mode-locked (STML) in the multimode fiber laser [4], unprecedently increasing attention has been drawn as it exhibits to be a promising scheme towards generating high-energy femtosecond pulses [5,6]. The three-dimensional (3D) soliton inherited from the multimode fibers can provide additional degrees of freedom that are promising for various applications [7,8], e.g., nonlinear frequency conversion [9] and spatial multiplexing for dual-comb generation [10]. From the

perspective of fundamentals of physics, 3D soliton is one of the 3D optical analogues that can be underpinned by the generic Gross-Pitaevskii equation [11], and shows the potential for interdisciplinary studies of Bose-Einstein condensates [12,13]. While, its extended concept – 3D dissipative soliton that intrinsically prevails in STML multimode fiber laser enables to access the rich 3D nonlinear optical physics [14], like soliton molecules [15,16], self-similar pulses [17], optical rogue waves [18], Q-switching dynamics [19], period-doubling bifurcations [20], spatiotemporal instability [21] and spatial beam cleaning [22,23].

Although many experimental studies of the STML dynamics have been demonstrated, the theoretical understanding of their physics is still limited [24-30]. To this end, L. Wright et al. recently proposed an attractor dissection theory for dissecting the intracavity effects responsible for forming 3D dissipative soliton [31,32]. Soon after, the STML laser using a step-index multimode fiber that has a large modal dispersion [33] was implemented, and the underlying mechanism was discussed afterwards [34], in which the interaction between the spatiotemporal saturable absorption (SA) and spatial gain competition was analyzed. It is noticed that the theoretical modeling by far mostly hinges on the generalized multimode nonlinear Schrödinger equation (GMMNLSE), wherein a Gaussian gain shaping is adopted at each spatial point of the mode field, i.e., termed as Gaussian-gain model [4,7,14,31,33,34]. Despite the simplicity, it fails to include several ingredients essential for these spatiotemporal dynamics that are commonly observed in experiments, such as pump depletion, spatial gain saturation, and explicit gain filtering [35]. To this end, a supplementary model for STML lasers that leverages the multimode rate equation (MMRE) is highly desired [36-38], as its feasibility has been verified by the unidirectional propagation of 3D solitons in a multimode fiber amplifier, which involves spatiotemporal deterioration [39] and beam self-cleaning [35].

In this work, we present a comprehensive model for studying the intracavity nonlinear dynamics of STML multimode fiber lasers by exploring the dynamic multimode gain in a framework of integrating the mode-resolved MMRE with GMMNLSE. Using this new model of the STML laser, the attractor dissection theory is revisited to investigate the modal dynamics of the 3D dissipative soliton. Specifically, as the 3D dissipative soliton circulates in the STML cavity modeled with dynamic multimode gain, different gain dynamics can yield distinct types of gain attractors, resulting in two operation regimes of STML that are dominated by the multimode gain effect and spatiotemporal SA, respectively. In the latter regime, particularly, the 3D dissipative soliton presents bistability — bifurcated solutions with two different linearly polarized (LP) mode compositions, i.e., LP₀₁ mode and LP₁₁ mode, respectively. In the experiment, we further confirmed the switching between LP₀₁ and LP₁₁ modes. The proposed dynamic multimode gain model of STML multimode fiber lasers might open new opportunities for fully studying the spatiotemporal dynamics of 3D dissipative solitons.

2. Dynamic multimode gain model of STML multimode fiber laser

Figure 1 conceptionally illustrates the modeling of the STML multimode fiber laser that leverages dynamic multimode gain. As shown in Fig. 1(a), the STML cavity mainly consists of a multimode gain fiber (MMGF), a SA and an optical coupler (OC). The MMGF is modeled as a quasi-three-level system in the framework of GMMNLSE with mode-resolved MMRE, which can fully interpret the multimode gain dynamics interplayed with nonlinear modal coupling. Here, the MMGF is a step-index multimode Yb³⁺-doped fiber (YDF) that has a core diameter of 20 μm . In the modeling, six transverse modes (TMs) are considered, including LP₀₁, LP_{11a}, LP_{11b}, LP_{21a}, LP_{21b}, and LP₀₂. To understand the fundamental mechanism of generating stable 3D dissipative solitons, the attractor dissection theory is associated with this new model to analyze the modal compositions of eigenpulses with respect to the gain operator (\hat{G}) and a joint effect operator ($\hat{D} + \hat{SA}$, \hat{D} and \hat{SA} account for the dispersion and SA effect, respectively), as depicted in Fig. 1(b). Under the interplay between the \hat{G} and $(\hat{D} + \hat{SA})$ attractors, the formation of 3D dissipative solitons in the laser cavity can be divided into two regimes (i and ii), led by multimode gain effect and spatiotemporal SA, respectively. In regime i, the LP₀₁ mode

dominates the gain extraction process, resulting in monostability. In regime ii, the multimode gain is homogenized for different spatial modes, and the presence of $(\hat{D} + \hat{SA})$ attractors gives rise to the bistability (to be discussed).

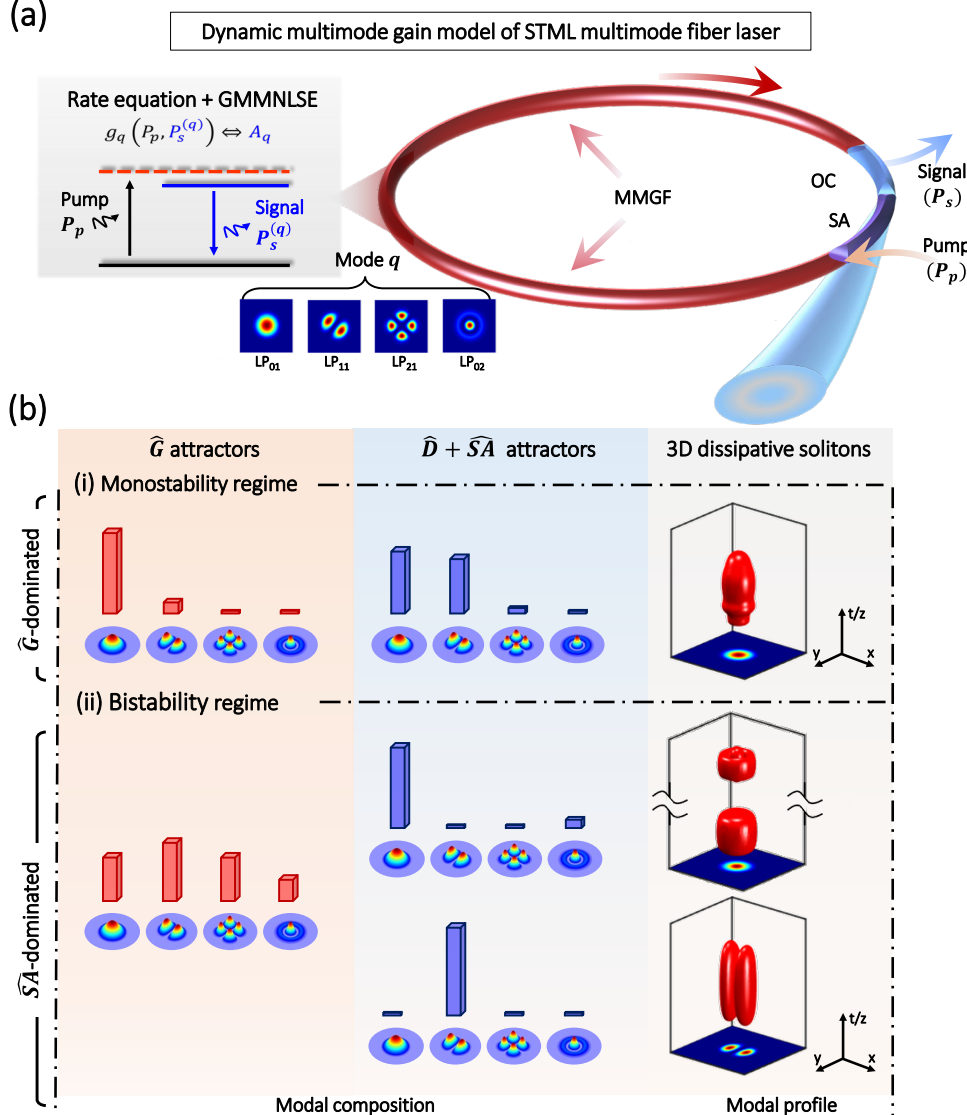


Fig. 1. Dynamic multimode gain model of spatiotemporal mode-locked (STML) multimode fiber laser. (a) Schematic diagram of the STML multimode fiber laser. The dynamic multimode gain of the multimode gain fiber (MMGF) is modeled by the generalized multimode nonlinear Schrödinger equation (GMMNLSE) that is associated with the multimode rate equation (MMRE). Here, six transverse modes (TMs, including two pairs of degenerate modes) are considered in the numerical study. OC: optical coupler; SA: saturable absorption. (b) Formation of 3D dissipative solitons in the STML multimode fiber laser. Here, the 3D dissipative solitons are generated by the combined role of \hat{G} and $(\hat{D} + \hat{SA})$, wherein \hat{G} , \hat{D} , and \hat{SA} represent the operators of gain, dispersion, and SA, respectively. Two regimes, i.e., (i) monostability and (ii) bistability dominated by the multimode gain effect and spatiotemporal SA, respectively. The height of the red and blue bars quantifies the modal compositions of the \hat{G} and $(\hat{D} + \hat{SA})$ attractors, respectively.

A. Dynamic multimode gain

In the framework of GMMNLSE characterizing the propagation of 3D dissipative solitons within the multimode fiber laser cavity using a MMGF, the gain function g_q is described by the mode-resolved MMRE, which contrasts with the multimode gain presented in full-field formalism [4,31]. Specifically, a set of multimode propagation equations can be expressed in the forms of

$$\frac{dP_p(z)}{dz} = \Gamma_p (\sigma_{ep} n_2(z) - \sigma_{ap} n_1(z)) P_p(z), \quad (1)$$

$$\begin{aligned} \frac{dP_s^{(q)}(z, \lambda_k)}{dz} = & \sigma_{es}(\lambda_k) \left[P_s^{(q)}(z, \lambda_k) + 2h \frac{c^2}{\lambda_k^3} \Delta\lambda \right] \Gamma_s^{(q)} n_2(z) \\ & - \sigma_{as}(\lambda_k) P_s^{(q)}(z, \lambda_k) \Gamma_s^{(q)} n_1(z), \end{aligned} \quad (2)$$

where, $P_p(z)$ and $P_s^{(q)}(z, \lambda_k)$ represent the z -dependent pump power and signal power of the spatial mode q at the wavelength of λ_k . n_2 and n_1 denote the population densities of Yb^{3+} ions at the upper and lower energy levels, respectively. More details about the dynamic multimode gain model are provided in Sec. S1.1 of Supplemental Material [40], and the definitions and values of key parameters are summarized in Table S1.

From Eq. (2), we arrive at an expression of the mode-resolved gain function g_q , i.e.,

$$g_q(\omega_k; z) = \Gamma_s^{(q)} (\sigma_{es}(\lambda_k) n_2(z) - \sigma_{as}(\lambda_k) n_1(z)). \quad (3)$$

B. Attractor dissection

To unveil the key intracavity effects responsible for generating the 3D dissipative soliton in the proposed dynamic multimode gain model, the attractor dissection theory is leveraged to evaluate the two principal ingredients, i.e., the mode-resolved gain and SA effect. These two effects are regarded as projection operators that represent the transformations of the optical field envelopes [31], and the corresponding field attractors $A(x, y, t)$ (also understood as ‘eigenpulses’) with respect to the operators can be expressed as

$$A_q^G(t) = \lim_{n \rightarrow \infty} [\hat{R} \hat{G}]^n E_q^0(t), \quad (4)$$

$$A^{SA}(x, y, t) = \lim_{n \rightarrow \infty} [\hat{R} \hat{S} \hat{A} \hat{D}]^n E^0(x, y, t), \quad (5)$$

where, A_q^G and A^{SA} are the eigensolutions with regard to the MMGF and SA. \hat{R} is a rescaling operator to retain the total energy. $E_q^0(t)$ and $E^0(x, y, t)$ are the initial fields in the mode-resolved and full-field formalisms, respectively. A full description of the attractor dissection theory can be found in the Sec. S1.2 of Supplemental Material [40]. For intuitive understanding, Fig. 1(b) showcases two representative modal compositions of the \hat{G} and $(\hat{D} + \hat{S} \hat{A})$ attractors. Regarding the attractor, there are several noteworthy aspects: (1) the use of operator \hat{G} provides an approximate way to describe the propagation of 3D dissipative solitons in the MMGF, although it is too complicated in reality to unveil the interplay between the multimode gain, spatiotemporal dispersion and nonlinear modal coupling (also discussed in Sec. S2 of Supplemental Material [40]); (2) the modal composition of the field attractor is interpreted as the energy distribution of the TM families. In this way, the spatiotemporal dispersion and nonlinear modal coupling less influence the modal dynamics and thus justify the use of operator \hat{G} (see Sec. S2.2 of Supplemental Material for more details [40]); (3) the modal dispersion is crucial to assess the $\hat{S} \hat{A}$ attractor and achieve convergence, since the induced temporal walk-off effect may influence the operator $\hat{S} \hat{A}$; (4) the field attractor, particularly $\hat{S} \hat{A}$, can manifest the multistability and is then, to some extent, susceptible to the initial condition.

3. Bistability dynamics of 3D dissipative soliton governed by dynamic multimode gain

A. Transition from monostability to bistability

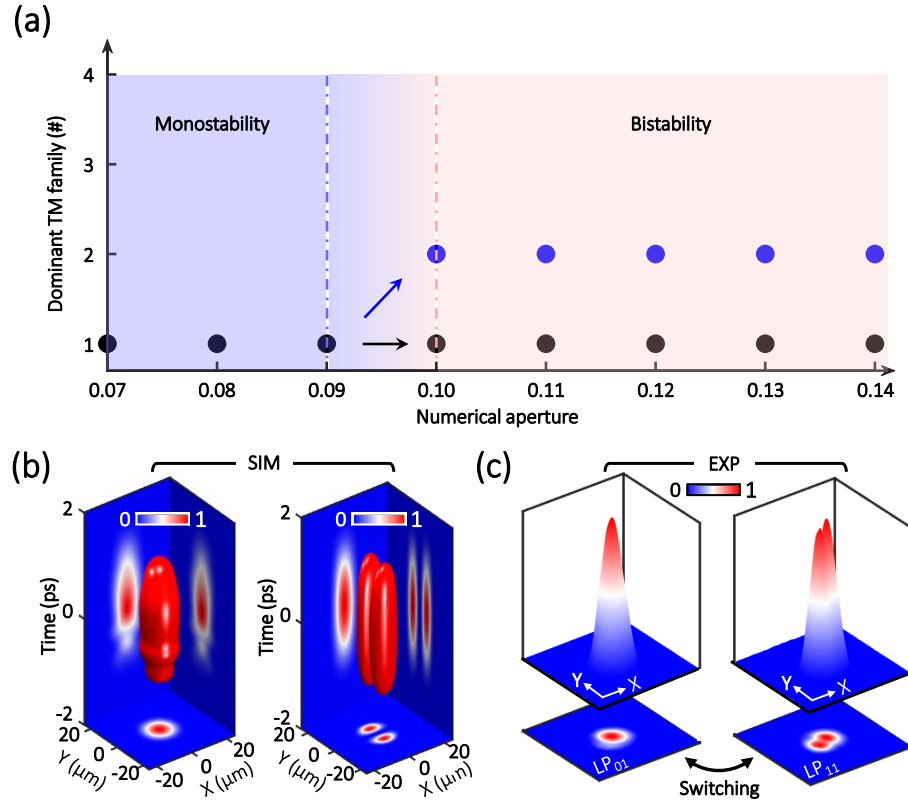


Fig. 2. Spatiotemporal dynamics of 3D dissipative soliton in the STML multimode fiber laser with dynamic multimode gain. (a) Dominant spatial modes of the 3D dissipative soliton as the numerical aperture (NA) of the MMGF varies from 0.07 to 0.14. The monostability and bistability regimes are recognized, revealing that 3D dissipative soliton bifurcates from a single attractor (stable node) to pairwise attractors, as it is susceptible to the initial conditions. Here, the TM families 1, 2, 3, and 4 correspond to LP₀₁, LP₁₁, LP₂₁, and LP₀₂ modes, respectively. (b) Spatiotemporal profiles of the 3D dissipative solitons for NA = 0.07 (left) and 0.14 (right), respectively. The 3D isosurface plots of the spatiotemporal profiles are set to 10% of the peak intensity. (c) Beam profiles of bistability states in the experiment. The LP₀₁ and LP₁₁ modes can be experimentally switched between each other according to the initial conditions.

By utilizing the proposed dynamic multimode gain model, we here explore the generation of 3D dissipative solitons in the STML multimode fiber laser. Consistent with the propagation in MMGF (see details in Sec. S2 of Supplemental Material [40]), the numerical aperture (NA) of the MMGF is varied to access distinctive multimode gain characteristics and unveil the underlying mechanism of the spatiotemporal dynamics of generating 3D dissipative solitons. Fig. 2(a) shows that two distinguishing regimes, which are featured by monostability and bistability, respectively, are identified as the NA of the MMGF varies from 0.07 to 0.14, while the corresponding numerical results are provided in Sec. S3 of Supplemental Material [40]. Specifically, when the fundamental mode dominates the gain extraction interpreted by the \hat{G} attractor, the modal dynamics exhibit a monopolistic state dominated by the LP₀₁ mode, termed as the monostability regime. When the gain competition between modes is strong, the modal dynamics present two states wherein the LP₀₁ or LP₁₁ modes prevail over other spatial modes, termed as the bistability regime. Regarding a dissipative 3D system, the modal dynamics of the 3D dissipative soliton in the phase space manifest two domains. The first domain is defined by the initial conditions that asymptotically approach the LP₀₁-dominated attractor, and such convergence holds for all NA values in the range of [0.07, 0.14], as denoted by the black arrow in Fig. 2(a). The second domain behaves as a local bifurcation, while the spatial mode LP₀₁ interchanges its stability with LP₁₁ once the multimode gain exhibits a relatively uniform distribution, as denoted by the blue arrow in Fig. 2(a). The spatiotemporal characteristics of the

two attractors are further illustrated in Fig. 2(b). The LP₀₁ mode, together with weak LP₀₂ mode with a considerably low energy ratio, represents the first attractor, which can also be identified by the 3D isosurface plot shown in the left panel of Fig. 2(b). For the second attractor, the 3D isosurface plot identifies a single-LP₁₁ modal composition in the right panel Fig. 2(b), i.e., the degenerate LP_{11a} and LP_{11b} modes with energy ratios of 0.18 and 0.82, respectively. Then, a STML multimode fiber laser is implemented to explore the bistability dynamics, and we observe the switching process between the LP₀₁ and LP₁₁ modes in the STML state, with their beam profiles shown Figs. 2(c). More experimental details are provided in the Sec. S4 of Supplemental Material [40].

B. Mechanism based on attractor dissection theory

To gain more insight into the spatiotemporal dynamics of the 3D dissipative solitons with dynamic multimode gain, we focus on two typical cases with NA = 0.07 and 0.14, i.e., corresponding to the monostability and bistability regimes, respectively. In the monostability regime with NA = 0.07, the evolution of the energy distribution of the TM families is shown in Fig. 3(a), wherein it presents a rapid modal convergence towards the LP₀₁ mode, which can be verified by a near-Gaussian beam profile at roundtrip (RT) #2, as shown in the inset of Fig. 3(a). It is noticed that the LP₀₁ mode sheds a small fraction of energy into the LP₀₂ mode through the inter-LP-mode FWM. To understand such modal dynamics, we access the intracavity evolution of the energy distribution in the early stage of the RT evolution, i.e., RTs #2 and #3 in this case. The left panel of Fig. 3(b) illustrates the variation of the mode components (only the LP₀₁ and LP₁₁ modes are shown here) as the 3D dissipative soliton passes through each cavity element, i.e., MMGF, OC and SA. The results identify that there exist two important processes responsible for the beam shaping: 1) in the MMGF, the fundamental mode LP₀₁ has advantages in the energy extraction, and thus prevails in the gain competition by continuously increasing its energy ratio. After passing through the OC and SA, the 3D dissipative soliton experiences a significant energy amplification for cavity-loss compensation, in which the energy ratio is further increased in the second MMGF; 2) the spatiotemporal SA accompanies with the multimode gain dynamics to increase the energy ratio of the LP₀₁ mode. As a complementary approach, the attractor dissection theory that is useful for tracing the crucial intracavity effects [31] can be applied. The right panel of Fig. 3(b) shows the acquired field attractors of the operators \hat{G} and $(\hat{D} + \hat{S}\hat{A})$, such that the energy distributions of the TM families can be quantified. The calculated LP₀₁-dominated attractor suggests that the multimode gain (i.e., the operator \hat{G}) plays a decisive role in the spatial shaping, while the SA [i.e., the operator $(\hat{D} + \hat{S}\hat{A})$] accelerates this process. In contrast to the modal shaping of the 3D dissipative soliton influenced by the interplay between multimode gain and SA, the temporal shaping of the 3D dissipative soliton that entails intensity discrimination can be merely realized by the SA. Fig. 3(c) illustrates the spatiotemporal profiles (3D isosurface plots) of the 3D dissipative solitons at RTs #3, 5, 10, and 30. The temporal shaping of the 3D dissipative soliton is asynchronous with that of modal shaping (see projections on the y - t and x - t planes), i.e., lagging behind until RT #30. It is intriguing to recognize this asynchronous spatial and temporal shaping of the 3D dissipative soliton in a multimode fiber laser.

In the bistability regime with NA = 0.14, different initial conditions can probe different steady states of the 3D dissipative solitons. Figs. 4(a) and (b) show the evolutions of the energy distributions. It is worth noting that the energy distributions of the TM families similarly evolve in the beginning, but diverge after RT #4, yielding distinguishing beam profiles, as shown in the insets of Figs. 4(a) and (b). To clarify its origin, the intracavity evolution of the energy ratios of the LP₀₁ and LP₁₁ modes are shown in the left panels of Figs. 4(c) and (d). In contrast to the case shown in Fig. 3, here the multimode gain plays a trivial role in the modal dynamics of the 3D dissipative soliton, while the spatiotemporal SA mainly leads to the abrupt change of the energy ratios of the LP₀₁ and LP₁₁ modes. The above results suggest that the SA plays a

dominant role in the bistability of the STML laser. From the perspective of physical understanding, it is interesting to dissect the versatility of the SA. To this end, the full-field light fields extracted from RTs #4 and #5 are employed as the initial conditions $E^0(x, y, t)$ for calculating the field attractors of the operator $(\hat{D} + \hat{S}\hat{A})$, respectively. In the meantime, the field attractors of the operator \hat{G} are calculated when weak noisy fields are employed as the initial conditions in the dynamic multimode gain model. As showcased in the right panels of Figs. 4(c) and (d), the \hat{G} attractors exhibit similar modal components, while the $(\hat{D} + \hat{S}\hat{A})$ attractors present dramatically different energy distributions. The numerical simulations using the dynamic multimode gain model, denoted as SIM in Figs. 4(c) and (d), indicate a good consistency with that of the $(\hat{D} + \hat{S}\hat{A})$ attractor, suggesting that the bistability of the 3D dissipative soliton is originated from the multistable nature of the spatiotemporal SA.

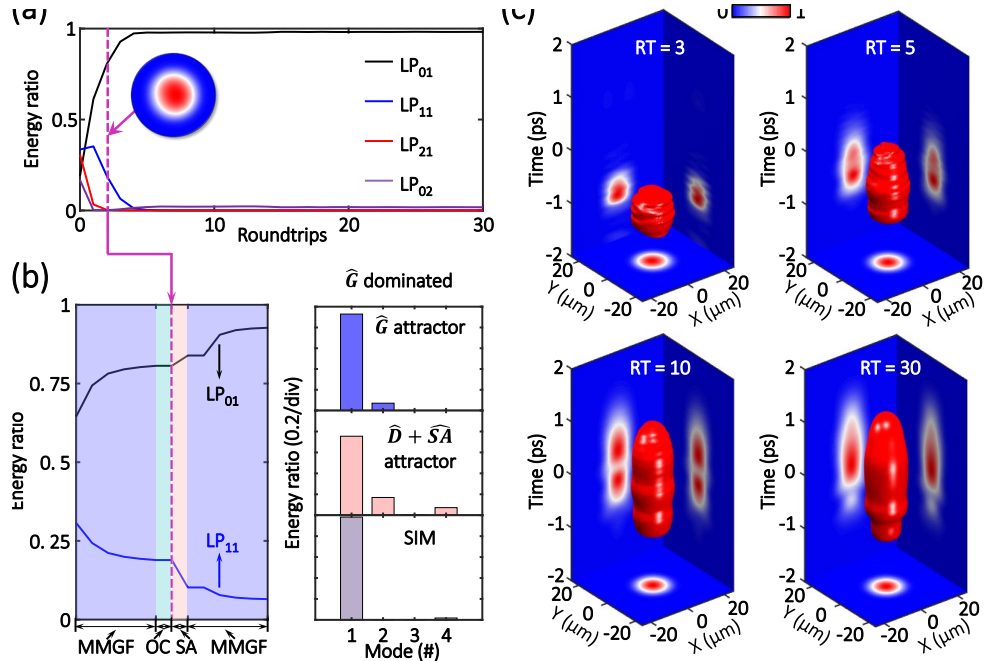


Fig. 3. Spatiotemporal dynamics of the 3D dissipative soliton generated from a MMGF with NA = 0.07. (a) Evolution of the energy distribution of the TM families. Inset depicts the beam profile at roundtrip (RT) #2. (b) Intracavity evolution of the energy ratios of the LP₀₁ and LP₁₁ modes (left panel). Right panel shows that the modal compositions of the 3D dissipative soliton in simulation (labeled by SIM), \hat{G} and $(\hat{D} + \hat{S}\hat{A})$ attractors. The results extracted from the OC at RT #2 are indicated by the dashed lines in (a) and (b). The MMGF, OC and SA are the components of the STML multimode fiber laser. Note that, the second MMGF belongs to the next RT, i.e., RT #3. (c) RT-evolving spatiotemporal profiles of the 3D dissipative soliton in the buildup state.

In the bistability regime with NA = 0.14, different initial conditions can probe different steady states of the 3D dissipative solitons. Figs. 4(a) and (b) show the evolutions of the energy distributions. It is worth noting that the energy distributions of the TM families similarly evolve in the beginning, but diverge after RT #4, yielding distinguishing beam profiles, as shown in the insets of Figs. 4(a) and (b). To clarify its origin, the intracavity evolution of the energy ratios of the LP₀₁ and LP₁₁ modes are shown in the left panels of Figs. 4(c) and (d). In contrast to the case shown in Fig. 3, here the multimode gain plays a trivial role in the modal dynamics of the 3D dissipative soliton, while the spatiotemporal SA mainly leads to the abrupt change of the energy ratios of the LP₀₁ and LP₁₁ modes. The above results suggest that the SA plays a dominant role in the bistability of the STML laser. From the perspective of physical understanding, it is interesting to dissect the versatility of the SA. To this end, the full-field

light fields extracted from RTs #4 and #5 are employed as the initial conditions $E^0(x, y, t)$ for calculating the field attractors of the operator $(\widehat{D} + \widehat{SA})$, respectively. In the meantime, the field attractors of the operator \widehat{G} are calculated when weak noisy fields are employed as the initial conditions in the dynamic multimode gain model. As showcased in the right panels of Figs. 4(c) and (d), the \widehat{G} attractors exhibit similar modal components, while the $(\widehat{D} + \widehat{SA})$ attractors present dramatically different energy distributions. The numerical simulations using the dynamic multimode gain model, denoted as SIM in Figs. 4(c) and (d), indicate a good consistency with that of the $(\widehat{D} + \widehat{SA})$ attractor, suggesting that the bistability of the 3D dissipative soliton is originated from the multistable nature of the spatiotemporal SA.

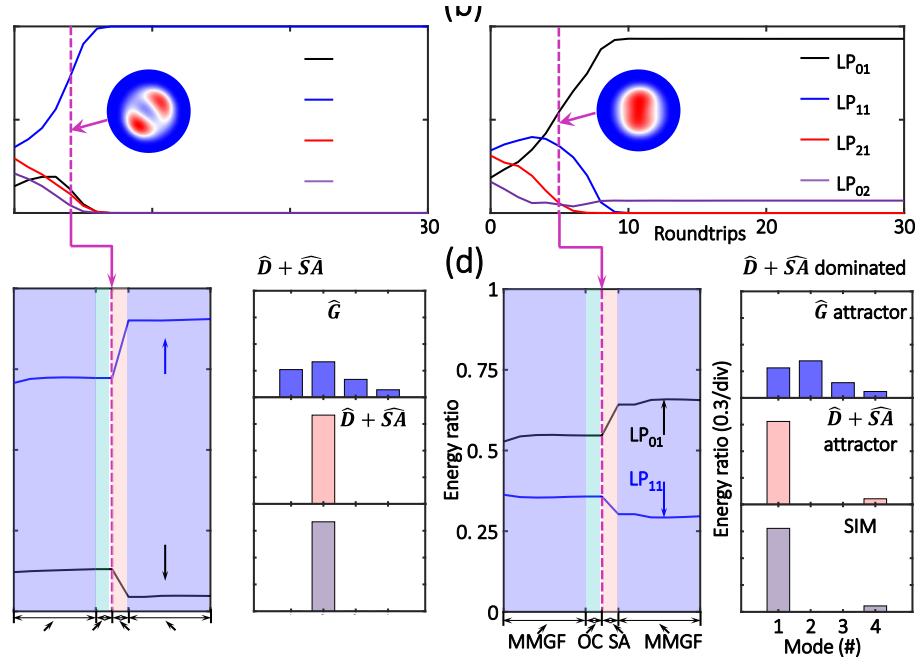


Fig. 4. Spatiotemporal dynamics of the 3D dissipative solitons generated from a MMGF with NA = 0.14. (a,b) Evolutions of the energy distributions of the TM families for two different 3D dissipative solitons that are dominated by LP₁₁ (a) and LP₀₁ (b) modes, respectively. Insets depict the beam profiles at RTs #4 and #5 of the two cases, respectively. (c,d) Intracavity evolutions of the energy ratios of the LP₀₁ and LP₁₁ modes (left panel). Right panels show that modal compositions of the 3D dissipative solitons in the simulation (labeled by SIM), \widehat{G} and $(\widehat{D} + \widehat{SA})$ attractors. The results extracted from the OC at RT #4 and #5 are indicated by the dashed lines in (a,c) and (b,d), respectively.

4. Conclusion and outlook

In conclusion, we comprehensively explore the spatiotemporal dynamics in STML multimode fiber laser by developing a dynamic multimode gain model that leverages MMRE and GMMNLSE. To unveil the formation mechanism of the 3D dissipative soliton, we revisit the attractor dissection theory to identify the roles of key intracavity ingredients in the shaping of 3D dissipative solitons, including the multimode gain and spatiotemporal SA. Specifically, via varying the NA of the MMGF, diverse gain dynamics, as well as different gain attractors are revealed, giving rise to two operation regimes — governed by multimode gain effect and spatiotemporal SA, respectively. The transition mechanism from monostability to bistability is then theoretically and experimentally investigated, and the bifurcated solutions with two distinct LP mode compositions, i.e., LP₀₁ and LP₁₁ modes, are identified. The proposed dynamic multimode gain model opens up new possibilities for investigating the spatiotemporal

dynamics of 3D dissipative solitons in multimode fiber lasers, and understanding the other 3D dissipative system.

Funding. This work was partially supported by National Natural Science Foundation of China (NSFC) (62375087 and 12374304), Key-Area Research and Development Program of Guangdong Province (2023B0909010002), NSFC Development of National Major Scientific Research Instrument (61927816), Introduced Innovative Team Project of Guangdong Pearl River Talents Program (2021ZT09Z109), Natural Science Foundation of Guangdong Province (2021B1515020074), and Science and Technology Project of Guangdong (2020B1212060002).

Disclosures. The authors declare no conflict of interest.

Data availability. Data underlying the results presented in this paper are not publicly available at this time but may be obtained from the authors upon reasonable request.

References

1. D. Brida, G. Krauss, A. Sell, and A. Leitenstorfer, “Ultrabroadband Er:fiber lasers,” *Laser Photonics Rev.* **8**(3), 409–428 (2014).
2. J. Kim and Y. Song, “Ultralow-noise mode-locked fiber lasers and frequency combs: principles, status, and applications,” *Adv. Opt. Photon.* **8**(3), 465–540 (2016).
3. D. Côté and H. M. van Driel, “Period doubling of a femtosecond Ti:sapphire laser by total mode locking,” *Opt. Lett.* **23**(9), 715–717 (1998).
4. L. G. Wright, D. N. Christodoulides, and F. W. Wise, “Spatiotemporal mode-locking in multimode fiber lasers,” *Science* **358**(6359), 94–97 (2017).
5. W. Fu, L. G. Wright, P. Sidorenko, S. Backus, and F. W. Wise, “Several new directions for ultrafast fiber lasers [Invited],” *Opt. Express* **26**(8), 9432–9463 (2018).
6. B. Cao, C. Gao, K. Liu, X. Xiao, C. Yang, and C. Bao, “Spatiotemporal mode-locking and dissipative solitons in multimode fiber lasers,” *Light Sci. Appl.* **12**, 260 (2023).
7. J. C. Jing, X. Wei, and L. V. Wang, “Spatio-temporal-spectral imaging of non-repeatable dissipative soliton dynamics,” *Nat. Commun.* **11**, 2059 (2020).
8. Y. Guo, X. Wen, W. Lin, W. Wang, X. Wei, and Z. Yang, “Real-time multispeckle spectral-temporal measurement unveils the complexity of spatiotemporal solitons,” *Nat. Commun.* **12**, 67 (2021).
9. L. Wright, D. Christodoulides, and F. Wise, “Controllable spatiotemporal nonlinear effects in multimode fibers,” *Nat. Photon.* **9**, 306–310 (2015).
10. E. Lucas, G. Lihachev, R. Bouchand, N. Pavlov, A. Raja, M. Karpov, M. Gorodetsky, and T. J. Kippenberg, “Spatial multiplexing of soliton microcombs,” *Nat. Photon.* **12**, 699–705 (2018).
11. A. Fusaro, J. Garnier, K. Krupa, G. Millot, and A. Picozzi, “Dramatic acceleration of wave condensation mediated by disorder in multimode fibers,” *Phys. Rev. Lett.* **122**(12), 123902 (2019).
12. K. Krupa, A. Tonello, B. M. Shalaby, M. Fabert, A. Barthélémy, G. Millot, S. Wabnitz and V. Couderc, “Spatial beam self-cleaning in multimode fibres,” *Nat. Photonics* **11**, 237–241 (2017).
13. H. Pourbeiran, P. Sidorenko, F. O. Wu, N. Bender, L. Wright, D. N. Christodoulides, and F. Wise, “Direct observations of thermalization to a Rayleigh–Jeans distribution in multimode optical fibres,” *Nat. Phys.* **18**(6), 685–690 (2022).
14. L. G. Wright, F. O. Wu, D. N. Christodoulides, and F. W. Wise, “Physics of highly multimode nonlinear optical systems,” *Nat. Phys.* **18**(9), 1018–1030 (2022).
15. Y. Guo, W. Lin, W. Wang, R. Zhang, T. Liu, Y. Xu, X. Wei, and Z. Yang, “Unveiling the complexity of spatiotemporal soliton molecules in real time,” *Nat. Commun.* **14**, 2029 (2023).
16. K. Liu, X. Xiao, Y. Ding, H. Peng, D. Lv, and C. Yang, “Buildup dynamics of multiple solitons in spatiotemporal mode-locked fiber lasers,” *Photon. Res.* **9**(10), 1898–1906 (2021).
17. U. Teğin, E. Kakkava, B. Rahmani, D. Psaltis, and C. Moser, “Spatiotemporal self-similar fiber laser,” *Optica* **6**(11), 1412–1415 (2019).
18. U. Teğin, P. Wang, and L. V. Wang, “Real-time observation of optical rogue waves in spatiotemporally mode-locked fiber lasers,” *Commun. Phys.* **6**, 60 (2023).
19. K. Liu, X. Xiao, and C. Yang, “Observation of transition between multimode Q-switching and spatiotemporal mode locking,” *Photon. Res.* **9**(4), 530–534 (2021).
20. X. Xiao, Y. Ding, S. Fan, X. Zhang, and C. Yang, “Spatiotemporal period-doubling bifurcation in mode-locked multimode fiber lasers,” *ACS Photonics* **9**(12), 3974–3980 (2022).
21. Y. Sun, P. Rivas, C. Milián, Y. Kartashov, M. Ferraro, F. Mangini, R. Jauberteau, F. Talenti, and S. Wabnitz, “Robust three-dimensional high-order solitons and breathers in driven dissipative systems: a Kerr cavity realization,” *Phys. Rev. Lett.* **131**, 137201 (2023).
22. U. Tegin, B. Rahmani, E. Kakkava, D. Psaltis, and C. Moser, “Single-mode output by controlling the spatiotemporal nonlinearities in mode-locked femtosecond multimode fiber lasers,” *Adv. Photonics* **2**(5), 056005 (2020).

23. G. Fu, T. Qi, W. Yu, L. Wang, Y. Wu, X. Pan, Q. Xiao, D. Li, M. Gong, and P. Yan, “Beam self-cleaning of 1.5 μm high peak-power spatiotemporal mode-locked lasers enabled by nonlinear compression and disorder,” *Laser Photon. Rev.* **17**(7), 2200987 (2023).
24. J. Chen, W. Hong, and A. Luo, “Nonlinear dynamics of beam self-cleaning on LP_{11} mode in multimode fibers,” *Opt. Express* **30**(24), 43453–43463 (2022).
25. X. Wei, J. C. Jing, Y. Shen, and L. V. Wang, “Harnessing a multi-dimensional fibre laser using genetic wavefront shaping,” *Light Sci. Appl.* **9**, 149 (2020).
26. T. Mayteevarunyoo, B. A. Malomed, and D. V. Skryabin, “Spatiotemporal dissipative solitons and vortices in a multi-transverse-mode fiber laser,” *Opt. Express* **27**(26), 37364–37373 (2019).
27. V. L. Kalashnikov and S. Wabnitz, “Distributed Kerr-lens mode locking based on spatiotemporal dissipative solitons in multimode fiber lasers,” *Phys. Rev. A* **102**(2), 023508 (2020).
28. H. Zhang, Y. Zhang, J. Peng, X. Su, X. Xiao, D. Xu, J. Chen, T. Sun, K. Zheng, J. Yao, and Y. Zheng, “All-fiber spatiotemporal mode-locking lasers with large modal dispersion,” *Photon. Res.* **10**(2), 483–490 (2022).
29. B. Cao, C. Gao, Y. Ding, X. Xiao, C. Yang, and C. Bao, “Self-starting spatiotemporal mode-locking using Mamyshev regenerators,” *Opt. Lett.* **47**(17), 4584–4587 (2022).
30. M. Zitelli, V. Couderc, M. Ferraro, F. Mangini, P. Parra-Rivas, Y. Sun, and S. Wabnitz, “Spatiotemporal mode decomposition of ultrashort pulses in linear and nonlinear graded-index multimode fibers,” *Photon. Res.* **11**(5), 750–756 (2023).
31. L. G. Wright, P. Sidorenko, H. Pourbeyram, Z. M. Ziegler, A. Isichenko, B. A. Malomed, C. R. Menyuk, D. N. Christodoulides, and F. W. Wise, “Mechanisms of spatiotemporal mode-locking,” *Nat. Phys.* **16**, 565–570 (2020).
32. F. Ö. Ilday, “Mode-locking dissected,” *Nat. Phys.* **16**(5), 504–505 (2020).
33. Y. Ding, X. Xiao, K. Liu, S. Fan, X. Zhang, and C. Yang, “Spatiotemporal mode-locking in lasers with large modal dispersion,” *Phys. Rev. Lett.* **126**, 093901 (2021).
34. C. Gao, B. Cao, Y. Ding, X. Xiao, D. Yang, H. Fei, C. Yang, and C. Bao, “All-step-index-fiber spatiotemporally mode-locked laser,” *Optica* **10**(3), 356–363 (2023).
35. Y. H. Chen, H. Haig, Y. Wu, Z. Ziegler, and F. Wise, “Accurate modeling of ultrafast nonlinear pulse propagation in multimode gain fiber,” *J. Opt. Soc. Am. B* **40**(10), 2633–2642 (2023).
36. M. Gong, Y. Yuan, C. Li, P. Yan, H. Zhang, and S. Liao, “Numerical modeling of transverse mode competition in strongly pumped multimode fiber lasers and amplifiers,” *Opt. Express* **15**(6), 3236–3246 (2007).
37. Z. Jiang and J. R. Marcante, “Impact of transverse spatial-hole burning on beam quality in large-mode-area Yb-doped fibers,” *J. Opt. Soc. Am. B* **25**(2), 247–254 (2008).
38. L. Huang, L. Kong, J. Leng, P. Zhou, S. Guo, and X. Cheng, “Impact of high-order-mode loss on high-power fiber amplifiers,” *J. Opt. Soc. Am. B* **33**(6), 1030–1037 (2016).
39. G. Fu, D. Li, M. Gong, P. Yan, and Q. Xiao, “Spatiotemporal deterioration in nonlinear ultrafast fiber amplifiers”, *Appl. Phys. Lett.* **123**(9), 091106 (2023).
40. See Supplemental Material atfor other simulation details, MMGF amplification, and numerical results of soliton attractors.

Supplementary Materials

Bistability in spatiotemporal mode-locking with dynamic multimode gain

**ZHIJIN XIONG,^{1,3} YUANKAI GUO,^{1,3} WEI LIN,^{1,3} HAO XIU,¹ YUNCONG MA,¹
XUEWEN CHEN,¹ ZHAOHENG LIANG,¹ LIN LING,¹ TAO LIU,¹ XIAOMING WEI,^{1*}
AND ZHONGMIN YANG^{1,2*}**

¹*School of Physics and Optoelectronics, State Key Laboratory of Luminescent Materials and Devices,
Guangdong Engineering Technology Research and Development Center of Special Optical Fiber
Materials and Devices, Guangdong Provincial Key Laboratory of Fiber Laser Materials and Applied
Techniques, South China University of Technology, Guangzhou 510640, China*

²*Research Institute of Future Technology, South China Normal University, Guangzhou 510006, China*

³*These authors equally contributed to this work.*

**email:xmwei@scut.edu.cn; yangzm@scut.edu.cn*

Section S1. Detailed descriptions of dynamic multimode gain model and attractor dissection theory

This section provides full descriptions of the dynamic multimode gain model and attractor dissection theory. Note that, Eqs. (1-5) in the main text are repeated in the following for easy understanding.

S1.1 Dynamic multimode gain model

The generalized multimode nonlinear Schrödinger equation (GMMNLSE) is utilized to describe the propagation of three-dimensional (3D) solitons in the multimode fiber laser cavity using a multimode gain fiber (MMGF), i.e.,

$$\begin{aligned} \partial_z A_q(t; z) = & \frac{1}{2} \int_{-\infty}^{+\infty} g_q(\omega; z) \widetilde{A}_q(\omega; z) e^{-i\omega t} d\omega + i\delta\beta_0^{(q)} A_q - \delta\beta_1^{(q)} \partial_t A_q \\ & + \sum_{m=2}^3 i^{m+1} \frac{\beta_m^{(q)}}{m!} \partial_t^m A_q + i \frac{n_{2f}\omega_0}{c} \left(1 + \frac{i}{\omega_0} \partial_t\right) \sum_{l,m,n} S_{qlmn} A_l A_m A_n^*. \end{aligned} \quad (S1)$$

where $A_q(t; z)$ represents the electric field distribution of the linearly polarized (LP) spatial mode q , and its Fourier transform is described as $\widetilde{A}_q(\omega; z)$. $\delta\beta_0^{(q)}$ and $\delta\beta_1^{(q)}$ represent the differences of the propagation constant and inverse group velocity between the spatial mode q and fundamental mode, respectively. $\beta_m^{(q)}$ is the m^{th} -order dispersion coefficient of the mode q , and S_{qlmn} is the nonlinear coupling coefficient in the Kerr effect, wherein l, m, n are the indices of the transverse modes (TMs, including LP₀₁, LP_{11a}, LP_{11b}, LP_{21a}, LP_{21b}, and LP₀₂). n_{2f} accounts for the nonlinear refractive index of the fiber. ω_0 is the center frequency of the light field. c is the speed of light. In contrast to the multimode gain presented in full-field formalism [1,2], here the gain function g_q is mode-resolved in the multimode rate equation (MMRE) model. The steady-state MMRE can be simplified by substituting the mode-resolved overlapping factor $\Gamma_s^{(q)}$ for explicit transverse space integral, i.e.,

$$n_2(z) = n_{Yb} \frac{\frac{P_p(z)\Gamma_p\sigma_{ep}}{hv_p S_{core}} + \sum_q \sum_k \frac{P_s^{(q)}(z, \lambda_k)\Gamma_s^{(q)}\sigma_{es}(\lambda_k)}{hv_k S_{core}}}{\frac{1}{\tau} + \frac{P_p(z)\Gamma_p(\sigma_{ep} + \sigma_{ap})}{hv_p S_{core}} + \sum_q \sum_k \frac{P_s^{(q)}(z, \lambda_k)\Gamma_s^{(q)}(\sigma_{es}(\lambda_k) + \sigma_{as}(\lambda_k))}{hv_k S_{core}}}, \quad (S2)$$

with, $\Gamma_s^{(q)} = \frac{\int_{-\alpha_{core}}^{\alpha_{core}} \int_{-\alpha_{core}}^{\alpha_{core}} i^{(q)}(x, y) dx dy}{\int_{-\infty}^{+\infty} \int_{-\infty}^{+\infty} i^{(q)}(x, y) dx dy}$,

where $i^{(q)}(x, y)$ is the normalized modal-intensity distribution. A set of multimode propagation equations can be expressed in the forms of

$$\frac{dP_p(z)}{dz} = \Gamma_p (\sigma_{ep} n_2(z) - \sigma_{ap} n_1(z)) P_p(z), \quad (S3)$$

$$\begin{aligned} \frac{dP_s^{(q)}(z, \lambda_k)}{dz} = & \sigma_{es}(\lambda_k) \left[P_s^{(q)}(z, \lambda_k) + 2h \frac{c^2}{\lambda_k^3} \Delta\lambda \right] \Gamma_s^{(q)} n_2(z) \\ & - \sigma_{as}(\lambda_k) P_s^{(q)}(z, \lambda_k) \Gamma_s^{(q)} n_1(z). \end{aligned} \quad (S4)$$

From Eq. (S4), the mode-resolved gain function can be expressed as

$$g_q(\omega_k; z) = \Gamma_s^{(q)} (\sigma_{es}(\lambda_k) n_2(z) - \sigma_{as}(\lambda_k) n_1(z)). \quad (S5)$$

In Eqs. (S2-S5), $P_p(z)$ and $P_s^{(q)}(z, \lambda_k)$ represent the z -dependent pump power and signal power of the spatial mode q at the wavelength of λ_k , respectively. n_2 and n_1 denote the population densities of Yb^{3+} ions at the upper and lower energy levels, respectively. Definitions

and values of the key parameters are summarized in Table S1. The connection between $\widetilde{A}_q(\omega_k; z)$ in GMMNLSE and $P_s^{(q)}(z, \lambda_k)$ in MMRE is given as

$$P_s^{(q)}(z, \lambda_k) = \frac{|\widetilde{A}_q(\omega_k; z)|^2 f_{rep}}{T_{span}}, \quad (S6)$$

where T_{span} is the temporal window of the numerical simulation. The dynamic multimode gain model described by Eqs. (S1-S6) is numerically solved by a split-step method with a fourth-order Runge-Kutta algorithm [3]. A graphical processing unit (GPU) is employed to speed up the computation of the 3D numerical simulation.

The propagation of 3D light fields in the optical coupler (OC) and saturable absorption (SA) can be mathematically described as

$$A(x, y, t; L_{MMF}) = \sum_q F_q(x, y) A_q(t; L_{MMF}) / \sqrt{\iint |F_q(x, y)|^2 dx dy}, \quad (S7a)$$

$$A(x, y, t; L_{MMF}^+) \rightarrow A(x, y, t; L_{MMF}) \sqrt{1 - l_{OC}}, \quad (S7b)$$

$$A(x, y, t; 0) \rightarrow A(x, y, t; L_{MMF}^+) \sqrt{1 - \frac{1}{1 + |A(x, y, t)|^2 / I_{sat}}}, \quad (S7c)$$

where $A(x, y, t; z)$ represents the intracavity light field in full-field formalism and is calculated by involving the transverse-mode-field distribution $F_q(x, y)$ of the spatial mode q . $z = L_{MMF}$ and L_{MMF}^+ designate the positions of the OC and SA in the laser cavity, respectively. $A(x, y, t; 0)$ is the initial condition of the light field used for the iteration calculation.

Table S1. Key parameters used in the numerical simulation

Cavity	Value						
Fiber length (L_{MMF} , m)	1						
Repetition rate (f_{rep} , MHz)	200						
Output ratio of OC (l_{OC})	0.1						
Saturation intensity of SA (I_{sat} , GW/cm ²)	30						
Pump power ($P_p(0)$, W)	3						
Multimode gain fiber (MMGF)	Value						
Yb ³⁺ ion concentration (n_{Yb} , m ⁻³)	1×10^{26}						
Central wavelength of pump/signal (λ_p/λ_s , nm)	976/1050						
Absorption cross section at λ_p (σ_{ap} , m ²)	1.33×10^{-24}						
Emission cross section at λ_p (σ_{ep} , m ²)	1.325×10^{-24}						
Absorption cross section at λ_s ($\sigma_{as}(\lambda_s)$, m ²)	1.43×10^{-26}						
Emission cross section at λ_s ($\sigma_{es}(\lambda_s)$, m ²)	4.8×10^{-25}						
Core radius/area (α_{core}/S_{core} , $\mu\text{m}/\mu\text{m}^2$)	10/314.2						
Lifetime (τ , ms)	1.84						
Overlapping factor of pump (Γ_p)	0.01						
Overlapping factor of signal ($\Gamma_s^{(q)}$) (NA = 0.07)	<table border="1"> <tr> <td>LP₀₁ ($q = 1$)</td><td>0.95</td></tr> <tr> <td>LP₁₁ ($q = 2,3$)</td><td>0.86</td></tr> <tr> <td>LP₂₁ ($q = 4,5$)</td><td>0.70</td></tr> </table>	LP ₀₁ ($q = 1$)	0.95	LP ₁₁ ($q = 2,3$)	0.86	LP ₂₁ ($q = 4,5$)	0.70
LP ₀₁ ($q = 1$)	0.95						
LP ₁₁ ($q = 2,3$)	0.86						
LP ₂₁ ($q = 4,5$)	0.70						

	LP ₀₂ ($q = 6$)	0.52
	LP ₀₁ ($q = 1$)	0.99
Overlapping factor of signal ($\Gamma_s^{(q)}$) (NA = 0.14)	LP ₁₁ ($q = 2,3$)	0.98
	LP ₂₁ ($q = 4,5$)	0.96
	LP ₀₂ ($q = 6$)	0.95

S1.2 Attractor dissection theory

To unveil key intracavity effects responsible for generating 3D dissipative solitons in the proposed dynamic multimode gain model, the attractor dissection theory is leveraged to evaluate the two principal ingredients, i.e., the multimode gain and SA effect. These two effects are regarded as projection operators that represent the transformations of the optical field envelope [2] and the corresponding field attractors $A(x, y, t)$ (also understood as ‘eigenpulses’) with respect to the operators, i.e.,

$$A_q^G(t) = \lim_{n \rightarrow \infty} [\hat{R}\hat{G}]^n E_q^0(t), \quad (S8a)$$

$$A^{SA}(x, y, t) = \lim_{n \rightarrow \infty} [\hat{R}\hat{S}\hat{A}\hat{D}]^n E^0(x, y, t), \quad (S8b)$$

$$A_q^{SA}(t) = \iint F_q^*(x, y) A^{SA}(x, y, t) dx dy / \sqrt{\iint |F_q(x, y)|^2 dx dy}. \quad (S8c)$$

The modal composition is quantified by the energy ratios $\{\mathcal{E}_q\}$ of the spatial modes, i.e.,

$$\mathcal{E}_q = \int |A_q^{G/SA}(t)|^2 dt / \sum_q \int |A_q^{G/SA}(t)|^2 dt, \quad (S9)$$

where A^G and A^{SA} are the eigensolutions with regard to the MMGF and SA. The operators \hat{G} , $\hat{S}\hat{A}$, \hat{D} account for the mode-resolved multimode gain, SA, and dispersion, respectively. \hat{R} is a rescaling operator to retain the total energy. $E_q^0(t)$ and $E^0(x, y, t)$ are the initial fields in the mode-resolved and full-field formalism, respectively.

Section S2. Spatiotemporal dynamics of 3D light field governed by dynamic multimode gain in MMGF amplification

In this section, we investigate the dynamics of the 3D light field in the single-pass MMGF amplification by characterizing the dynamic multimode gain and nonlinear modal coupling, respectively. In this way, we identify inter-degenerate-mode four-wave-mixing (FWM) as the dominating nonlinear-coupling process, which indicates that nonlinear modal coupling and spatiotemporal dispersion barely influence the modal dynamics of 3D light field when only non-degenerate TM families are taken into account.

S2.1 Characterization of dynamic multimode gain

To better understand the effect of the operator \hat{G} in the MMGF, we first investigate the MMRE-governed multimode gain dynamics that accompany the nonlinear intermodal coupling described by GMMNLSE in the single-pass amplification of 3D light field. We perform numerical simulation of a single-pass multimode Yb³⁺-doped fiber (YDF, $L_{MMF} = 1$ m) by launching mode-resolved hyperbolic secant pulses. The pulse energy is evenly distributed to six TMs, i.e., energy ratio $\mathcal{E} \sim 0.17$ for each spatial mode. The key parameters utilized in the simulation are provided in Table S1. As the mode-resolved overlapping factors $\Gamma_s^{(q)}$ depend on the fiber's numerical aperture (NA), two NAs (i.e., 0.07, 0.14) are set to study the gain competition effect and the underlying modal dynamics influenced by the gain competition, spatial gain saturation, and nonlinear modal coupling. The simulated results are summarized in Fig. S1. To distinguish the full intermodal nonlinear coupling with nonlinear interactions between degenerate modes and inter-LP-mode nonlinear coupling, the energy distributions of the six TMs and TM families (i.e., LP₀₁, LP₁₁, LP₂₁, and LP₀₂) are analyzed.

For NA = 0.07, starting from an equalized energy distribution, the simulation results show an evident discrepancy between energy ratios of the TMs for a relatively low level of input per-spatial-mode average power. Before the onset of obvious gain saturation, the lower-order spatial modes advance in extracting gain because of a larger mode-resolved overlapping factor $\Gamma_s^{(q)}$, which can be understood as the overlap of mode field distribution and population inversion distribution [4] (see values in Table S1). As the average power of each spatial mode increases, the gain of the lower-order modes experiences stronger saturation. Regarding the efficient saturation energy is inversely proportional to $\Gamma_s^{(q)}$ [5], the discrepancy between energy ratios of TMs becomes smaller for higher input per-spatial-mode average power. To visualize such modal dynamics governed by the spatial gain saturation, the beam profiles for the input per-spatial-mode average powers of 0.2 and 2 W are shown in the insets of Fig. S1(a). In addition to the case incorporating nonlinear modal coupling, i.e., the solid circles in Figs. S1(a) and S1(c), the energy ratios of the modes are also computed by removing the nonlinear modal coupling (i.e., $S_{qlmn} = 0$), i.e., the dotted lines in Figs. S1(a) and S1(c). A good consistency between the case with and without nonlinear modal coupling suggests that the MMRE-governed gain prevails in determining the modal dynamics of the 3D dissipative soliton that propagates in the MMGF with a relatively lower NA, e.g., typical large-mode-area YDFs [6-8].

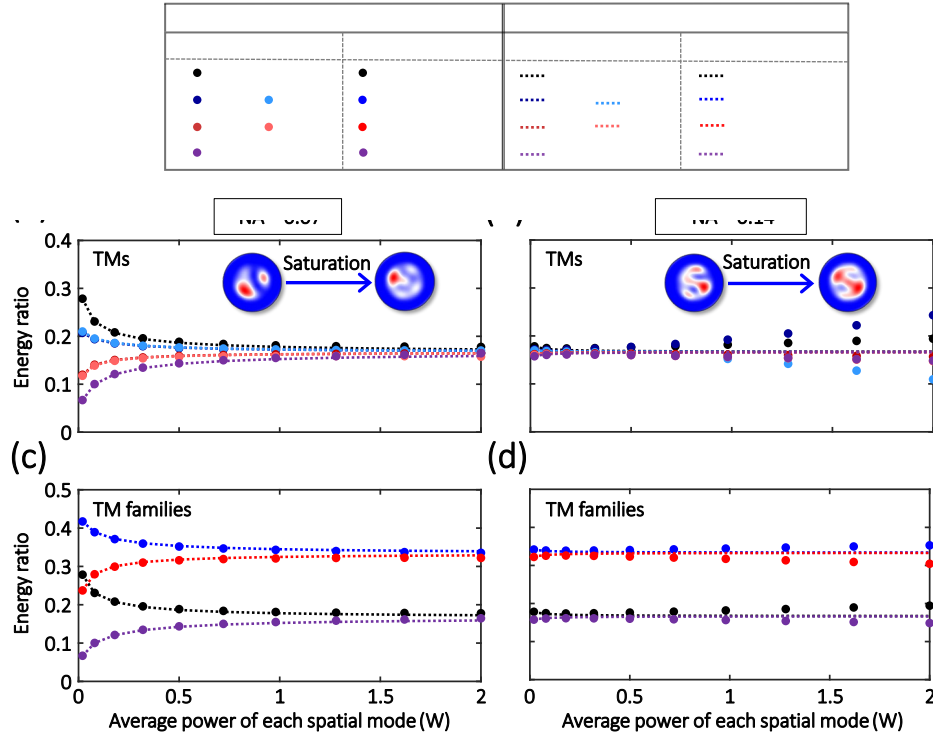


Fig. S1. Modal dynamics with varying input per-spatial-mode average powers. (a,c) Energy ratios of transverse modes (TMs) (a) and TM families (c) as a function of the input per-spatial-mode average power using 1-m multimode gain fiber (MMGF) with numerical aperture (NA) of 0.07. The solid circles and dotted lines represent the results with and without nonlinear modal coupling, respectively. Insets of (a) show the beam profiles at the input per-spatial-mode average powers of 0.02 W and 2 W, respectively. Note that, the results of TM families account for the superposition of the degenerate modes that start from an equalized energy distribution. (b,d) Energy ratios of TMs (b) and TM families (d) as a function of the input per-spatial-mode average power using 1-m MMGF with NA of 0.14.

When the NA increases to 0.14, the modal evolution as a function of input per-spatial-mode average power differs from the lower NA case, as shown in Figs. S1(b) and S1(d). In the unsaturated situation with low average power, the overlapping factors of the TMs are very close, i.e., 0.95~0.99 in Table S1. In this regard, the difference between the mode-resolved gains $\{g_q\}$, as well as the energy ratios of TMs, is small, as demonstrated in Fig. S1(b). By increasing the input per-spatial-mode average power, gain saturation arises, such that the critical role of the nonlinear modal coupling is identified by the pronounced deviation between the modal compositions that are calculated with and without nonlinear modal coupling. In contrast to the case of the TMs, the similar results for the TM families, as shown in Fig. S1(d), indicate a weaker deviation, leading to neglectable energy exchange between the non-degenerate modes. These results suggest that the nonlinear modal coupling is preferred to occur between the degenerate TMs (e.g., pairs of LP_{11a} and LP_{11b} , LP_{21a} and LP_{21b}) rather than the non-degenerate TM families (e.g., LP_{01} , LP_{11} , LP_{21} , LP_{02}). As a result, the inter-degenerate-mode FWM processes might primarily dominate the change of beam profile, as shown in the insets of Fig. S1(b).

S2.2 Characterization of nonlinear intermodal coupling

To identify the role of the nonlinear modal coupling in the spatiotemporal dynamics for the cases with higher NA, we further study the propagation of 3D dissipative solitons with $g_q(\omega; z) = 0$, in which way the multimode gain dynamics are isolated. In the numerical simulation, the initial signals are mode-resolved pulses with peak powers arbitrarily set in a

range of $[80^2, 120^2]$ watt. Fig. S2(a) shows a typical evolution of the energy distribution of the TM families as it propagates through the multimode fiber. There exist visible oscillations of the energy ratios in the early stage of evolution, except a weak modulation depth, which can be mainly attributed to the inter-LP-mode FWM before significant temporal walk-off between the pulses of the different TM families. For the TM families with degenerate modes, the evolutions of the energy ratios exhibit stronger oscillatory patterns; otherwise, variation of the energy ratio is inhibited due to the mismatches of propagation constant and group velocity, referring to $\beta_0^{(q)} = (0, -4, -4, -9.3, -9.3, -11.2) \text{ mm}^{-1}$ and $\beta_1^{(q)} = (0, 1.76, 1.76, 4, 4, 4.65) \text{ fs/mm}$. In the presence of modal dispersion, the inter-LP-mode FWM process is largely suppressed in the latter period of the pulses' propagation. The energy exchange between the non-degenerate TM families is prevented, which is in dramatic contrast to the case of the degenerate modes, like LP_{11a} and LP_{11b} , as illustrated in Fig. S2(b). The energy exchange between the degenerate modes gives rise to the rotation of the mode profile, as shown in the insets of Fig. S2(b). To verify the underlying mechanism of the intermodal energy exchange, we perform statistical calculations adopting signals with different initial conditions, and interpret the results in a quantitative way using L2 norm that is defined by input and output mode-resolved pulses, i.e., $L2 = \|\mathcal{E}^{in} - \mathcal{E}^{out}\|_2$, where the vectors \mathcal{E} of energy ratios are $(\mathcal{E}_1, \mathcal{E}_2, \mathcal{E}_3, \mathcal{E}_4, \mathcal{E}_5, \mathcal{E}_6)$ for the six TMs and $(\mathcal{E}_1, \mathcal{E}_2 + \mathcal{E}_3, \mathcal{E}_4 + \mathcal{E}_5, \mathcal{E}_6)$ for the four TM families, respectively. The remarkably smaller L2 norm for the non-degenerate TM families, as shown in Fig. S2(c), implies that the inter-LP-mode FWM serves a minor role in nonlinear modal coupling of the 3D soliton propagating in multimode fibers with a higher NA. Therefore, it is relatively rational to use the operator \hat{G} solely to characterize the dynamic multimode gain in MMGF amplification.

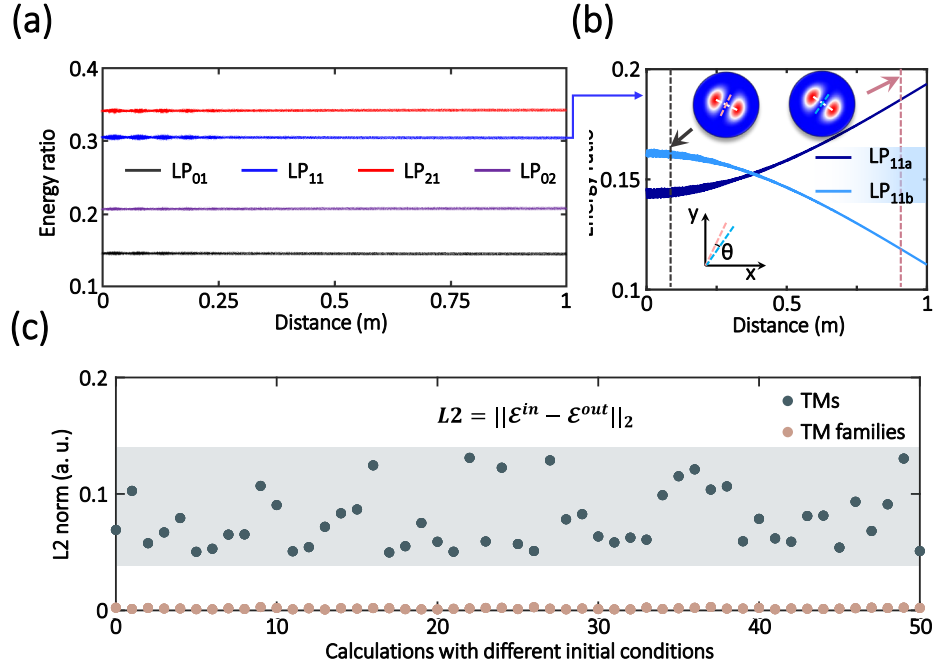


Fig. S2. Nonlinear modal coupling for a higher NA (i.e., $NA = 0.14$). (a) Evolution of the energy distribution of the TM families as the 3D soliton propagates through the 1-m MMGF. (b) Energy exchange between the degenerate modes of LP_{11a} and LP_{11b} . The top insets illustrate the beam profiles at the propagation distances of 0.1 m and 0.9 m, respectively. The bottom left inset shows the rotation of the beams' principal axes, as indicated in the top insets. (c) L2 norms that quantify the difference of modal compositions between input and output 3D solitons. Here, 50 calculations have been performed with different initial conditions, i.e., in each calculation, the peak powers of the mode-resolved hyperbolic-secant pulses are arbitrarily set in a range of $[80^2, 120^2]$ watt. The energy ratios \mathcal{E}^{in} and \mathcal{E}^{out} of input and output 3D solitons are obtained from Eq. (S9), and they are set as the entries of vectors for evaluating the L2 norms.

Section S3. Detailed numerical results of 3D dissipative soliton

In this section, we present the numerical results of 3D dissipative solitons in a spatiotemporal mode-locked (STML) multimode fiber laser when MMGF with varying NA is employed. To showcase the dynamics in the monostability and bistability regimes, modal compositions of 3D dissipative solitons in these two regimes are given in Tables S2 and S3, respectively.

Table S2. Numerical results of monostability

NA	TM families	Initial condition						
		Noise1	Noise2	Noise3	Noise4	Noise5	Noise6	Noise7
0.07	LP ₀₁	0.9823	0.9828	0.9823	0.9825	0.9826	0.9823	0.9820
	LP ₁₁	0	0	0	0	0	0	0
	LP ₂₁	0	0	0	0	0	0	0
	LP ₀₂	0.0177	0.0172	0.0177	0.0175	0.0174	0.0177	0.0180
0.08	...	0.9581	0.9602	0.9581	0.9612	0.9611	0.9605	0.9604
	...	0	0	0	0	0	0	0
	...	0	0	0	0	0	0	0
	...	0.0419	0.0398	0.0419	0.0388	0.0389	0.0395	0.0396
0.09	...	0.9531	0.9530	0.9530	0.9531	0.9529	0.9529	0.9530
	...	0	0	0	0	0	0	0
	...	0	0	0	0	0	0	0
	...	0.0469	0.0470	0.0470	0.0469	0.0471	0.0471	0.0470

Table S3. Numerical results of bistability

NA	TM families	Initial condition						
		Noise1	Noise2	Noise3	Noise4	Noise5	Noise6	Noise7
0.10	LP ₀₁	0.9458	0.9458	0	0.9458	0.9458	0.9457	0.9456
	LP ₁₁	0	0	1	0	0	0	0
	LP ₂₁	0	0	0	0	0	0	0
	LP ₀₂	0.0542	0.0542	0	0.0542	0.0542	0.0543	0.0544
0.11	...	0.9409	0.9409	0	0.9409	0.9409	0.9408	0.9407
	...	0	0	1	0	0	0	1
	...	0	0	0	0	0	0	0
	...	0.0591	0.0591	0	0.0591	0.0591	0.0592	0.0593
0.12	...	0.9374	0.9374	0	0	0.9375	0.9374	0.9374
	...	0	0	1	1	0	0	0
	...	0	0	0	0	0	0	0
	...	0.0626	0.0626	0	0	0.0625	0.0626	0.0626
0.13	...	0.9351	0.9352	0	0	0.9352	0.9351	0.9351
	...	0	0	1	1	0	0	0
	...	0	0	0	0	0	0	0
	...	0.0649	0.0648	0	0	0.0648	0.0649	0.0649
0.14	...	0.9347	0	0	0	0.9344	0	0
	...	0	1	1	1	0	1	1
	...	0	0	0	0	0	0	0
	...	0.0653	0	0	0	0.0656	0	0

Section S4. Experimental verification of bistability in STML multimode fiber laser

In this section, we first give a detailed description of the experimental setup and then address the implementation of bistability in practical situations.

S4.1 Experimental setup of the STML multimode fiber laser

The experimental setup of the STML multimode fiber laser is schematically shown in Fig. S3. The cavity configuration, incorporating both fiber and free-space components, is mainly made up by a segment of gain fiber, a semiconductor saturable absorber mirror (SESAM), a beam-splitter (BS), and an end mirror (M_1). Specifically, the gain fiber used is a 0.3-m-long step-index multimode Yb^{3+} -doped fiber (MMYDF, Nufern LMA-YDF-20/125-9M) with a 20- μm core diameter and a numerical aperture (NA) of 0.08, supporting up to about six TMs. The MMYDF is core-pumped by a 974-nm single-mode laser diode (SM-LD) with a maximum power of 900 mW. The pump light delivered by the SM-LD is collimated by a collimator (Col_1), subsequently passes through a mirror (M_2) and a long-pass dichroic mirror (LPDM), and is finally coupled into the MMYDF via another collimator (Col_2). The SESAM that acts as the other end reflector also imposes spatiotemporal SA upon the intracavity multimode light field. For more details, the adopted SESAM (Batop GmbH SAM-1040-27-1ps) has a modulation depth of 11%, a non-saturable loss of 16%, a relaxation time of 1 ps, and a saturation fluence of 30 $\mu\text{J}/\text{cm}^2$. The BS is inserted to render a 10% output for characterization. In addition, a mirror (M_3) is introduced to facilitate the cavity alignment; most importantly, adjusting the mirror M_3 can also influence the coupling from free space into the MMYDF and then equivalently induce a spatial filtering effect [6]. A combination of half- and quarter-wave plates is employed to fine tune the state of polarization (SOP) with respect to the 3D dissipative soliton.

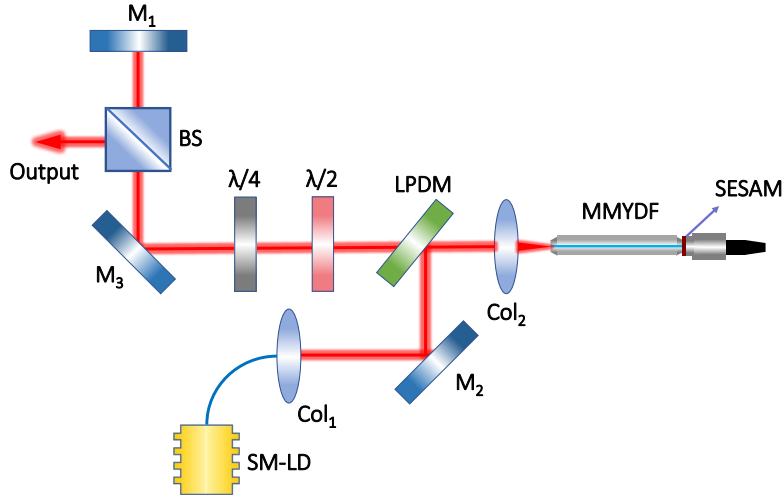


Fig. S3. Experimental setup of the spatiotemporal mode-locked (STML) multimode fiber laser. BS, beam splitter; Col, collimator; LPDM, long-pass dichroic mirror; $\lambda/2$ and $\lambda/4$ denote half- and quarter-wave plates, respectively; M, mirror; SM-LD, single-mode laser diode; SESAM, semiconductor saturable absorber mirror; MMYDF, multimode Yb^{3+} -doped fiber.

S4.2 Experimental implementation of bistability

Since the NA of the used MMYDF (i.e., $\text{NA}=0.08$) is slightly smaller than the critical value (i.e., $\text{NA}=0.1$) required for the onset of bistability. Thus, we address two noteworthy points to experimentally enter the bistability regime.

Consideration of the spatial filtering effect: here we equivalently tailor the modal composition of \hat{G} attractor by additionally considering a practical ingredient – spatial filter (i.e., the operator \hat{SF}) induced by the aforementioned coupling from free space into the MMYDF.

Hence, the \widehat{G} attractor is then substituted by a $(\widehat{G} + \widehat{SF})$ attractor which can be manipulated by adjusting the coupling condition. In this way, it is allowed to access the multimode gain with a relatively homogenized distribution, as demonstrated in Fig. S4. The obtained modal composition of the $(\widehat{G} + \widehat{SF})$ attractor closely resembles that of \widehat{G} attractor in the bistability regime [see Figs. 4(c) and (d) in the main text].

Adjusting the SOP: generally, in the single-mode scenario, similar soliton dynamics can be achieved by either restarting the mode-locked fiber laser or tuning the polarization [9]. Here, in the multimode counterpart, we introduce perturbations on the 3D dissipative soliton by fine tuning the wave plates, a slight variation of the SOP can potentially serve as the change of initial condition to probe a different steady state of the 3D dissipative soliton.

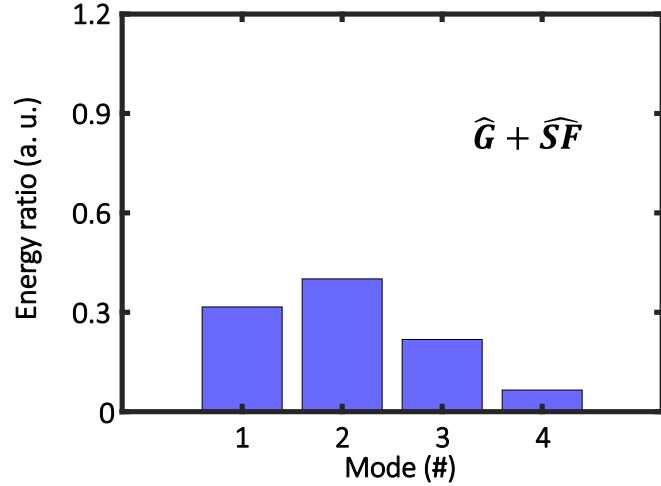


Fig. S4. Modal composition of the $(\widehat{G} + \widehat{SF})$ attractor. \widehat{G} and \widehat{SF} represent the operators of gain and spatial filter, respectively. In the numerical calculation, the modal coupling coefficients caused by the spatial filter are set as [0.4, 0.45, 0.45, 0.55, 0.55, 0.65].

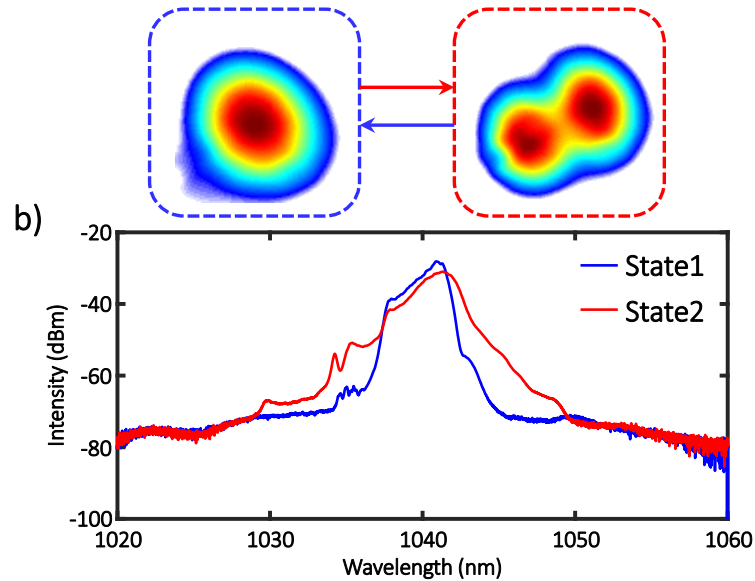


Fig. S5. Experimental results of the bistability in the STML operation. (a) Beam profiles of the bifurcated states (i.e., states 1 and 2). The blue and red dashed boxes represent the beam profiles of the LP_{01} -dominated state 1 and LP_{11} -

dominated state 2, respectively. (b) Corresponding optical spectra of the bifurcated states. The blue and red traces correspond to the states 1 and 2, respectively.

As stated above, in a situation by properly adjusting the spatial coupling, we increased the pump power to 700 mW and observed a LP₀₁-dominated state (termed as state 1 here) in the STML operation. The corresponding beam profile and optical spectrum are visualized in Fig. S5, and a high proportion of LP₀₁ mode can be identified. By slightly adjusting the SOP, we can obtain another state (referred to as state 2) in the STML operation, of which the LP₁₁ mode clearly dominates by viewing its beam profile [right panel of Fig. S5(a)]. The corresponding optical spectrum is also illustrated in Fig. S5(b). Therefore, we experimentally demonstrate the switching between LP₀₁ and LP₁₁ modes, and confirm the existence of the bistability in the STML multimode fiber laser.

Supplementary Reference

41. L. G. Wright, D. N. Christodoulides, and F. W. Wise, "Spatiotemporal mode-locking in multimode fiber lasers," *Science* **358**(6359), 94–97 (2017).
42. L. G. Wright, P. Sidorenko, H. Pourbeyram, Z. M. Ziegler, A. Isichenko, B. A. Malomed, C. R. Menyuk, D. N. Christodoulides, and F. W. Wise, "Mechanisms of spatiotemporal mode-locking," *Nat. Phys.* **16**, 565–570 (2020).
43. F. Poletti and P. Horak, "Description of ultrashort pulse propagation in multimode optical fibers," *J. Opt. Soc. Am. B* **25**(10), 1645–1654 (2008).
44. Z. Jiang and J. R. Marcante, "Impact of transverse spatial-hole burning on beam quality in large-mode-area Yb-doped fibers," *J. Opt. Soc. Am. B* **25**(2), 247–254 (2008).
45. Z. H. Huang, J. J. Wang, H. H. Lin, D. P. Xu, R. Zhang, Y. Deng, and X. F. Wei, "Combined numerical model of laser rate equation and Ginzburg–Landau equation for ytterbium-doped fiber amplifier," *J. Opt. Soc. Am. B* **29**, 1418–1423 (2012).
46. C. Gao, B. Cao, Y. Ding, X. Xiao, D. Yang, H. Fei, C. Yang, and C. Bao, "All-step-index-fiber spatiotemporally mode-locked laser," *Optica* **10**(3), 356–363 (2023).
47. G. Fu, D. Li, M. Gong, P. Yan, and Q. Xiao, "Spatiotemporal deterioration in nonlinear ultrafast fiber amplifiers", *Appl. Phys. Lett.* **123**(9), 091106 (2023).
48. Y. C. Liu, J. F. Wu, X. X. Wen, W. Lin, W. L. Wang, X. C. Guan, T. Qiao, Y. K. Guo, W. W. Wang, X. M. Wei, and Z. M. Yang, ">100 W GHz femtosecond burst mode all-fiber laser system at 1.0 μm," *Opt. Express* **28**, 13414–13422 (2020).
49. Y. Zhou, Y. X. Ren, J. W. Shi, and K. K. Y. Wong, "Breathing dissipative soliton explosions in a bidirectional ultrafast fiber laser," *Photon. Res.* **8**, 1566-1572 (2020).